Crystalline-Size Dependence of Dual Emission Peak on Hybrid Organic Lead Iodide Perovskite Films at Low Temperature

Raquel Chulia-Jordan[1,] *, Elena Mas-Marzá[2], Juan Bisquert[2,3], Juan P. Martínez-Pastor[1]

[1]Instituto de Ciencia de los Materiales, Universitat de València, 46071 Valencia, Spain

[2]Institute of Advamced Materials, Universitat Jaume I, 12006 Castelló, Spain

[3]King Abdullah University of Science and Technology (KAUST), Division of Physical Sciences and Engineering, Thuwal 23955-6900, Kindom of Saudi Arabia

Corresponding E-mail: raquel.chulia@uv.es

ABSTRACT: In this work, we have investigated the crystalline-size dependence of optical absorption and photoluminescence emission of $CH_3NH_3PbI_3$ films, which is necessary to identify the potencial practical applications of the gadgets based on perovskite films. This study was carried out at low temperatures to minimize the extra complexity induced by thermal effects. The purpose was clarifying the origin of the dual emission peak previously reported in literature. We have found that the grain-size is responsible of the appearance or disappearance of this dual emission on $CH_3NH_3PbI_3$ at low temperatures, whereas we have inferred that the thickness of the perovskite layer is a much more important factor than the size of the grains in the location of the energy of the bandgap. Moreover, the increase in the grain size allows slowing down the phase transition. Additionally, we evidence a decrease in the effective Rydberg energy of the exciton in several samples, from 23-25 meV at 7 K to 12-13 meV at 165 K, by fitting to Elliot-Toyozawa theory. We have extracted other important physical parameters of perovskites from the photoluminescence-data deconvolution, such as bandgap, exciton–phonon interaction and exciton binding energy. A new phase transition at 45.5 K was determined by the temperature dependence of full width at half maximum and integrated intensity of the photoluminescence, and it was confirmed by the radiative lifetime obtained from the time-resolved photoluminescence emission by mean of time-correlated single photon counting at different temperatures, excitation fluencies and emission energies.

1.- INTRODUCTION

Recently, a significant effort to understand the photophysical processes occurring in perovskites is being carried out, due to the potential that these materials offer to practical applications, such as solar cells, field effect transistors, lasers, batteries or light-emitting devices [1-5]. In particular, the organic-inorganic metal halide perovskite has been widely investigated because of the extraordinary improvement shown on the efficient solar cells. The unique properties of $CH_3NH_3PbI_3$, such as bandgap modulation or long-range balanced electron- and hole- diffusion lengths make it a promising photovoltaic material [6-8]. The structural stability and polymorphism of this material as a function of temperature (T) has been previously reported: cubic-tetragonal (327 K), tetragonal-orthorhombic (165 K). However, there are still some unsolved questions, about important photophysical processes occurring in $CH_3NH_3PbI_3$ films that need to be clarified, such as the origin of the dual emission peak already observed at low temperature [9]. Although its existence was previously shown, the scientific community has not come to an agreement about the origin of this dual emission. For example, Xing [10] reported three emission peaks, which have been assigned to two bound-exciton emissions and a free-exciton; however, Fang [11] attributed the low- and high-energy emission peaks to free and bound excitons and Kong [12] to a donor-acceptor pair (low energy) and free-exciton transitions, respectively. Lastly, Panzer [13] and Wehrenfennig [14] ascribed the existence of this dual emission to the presence of tetragonal inclusions in the orthorhombic phase at low temperature, whereas Dar [6] attributed it to the coexistence of $CH_3NH_3^+$-ordered and $CH_3NH_3^+$-disordered orthorhombic domains. Hence, despite the current effort, an understanding of the essential characteristics of perovskite films is still evolving.

Moreover, it has been studied how the thickness of the perovskite films affects the absorbance and the photocurrent. The absorption coefficient curve of the organometal halide perovskites ($CH_3NH_3PbX_3$, X = halogen) at room temperature showed not only an unusual sharp shoulder near its reported bandgap value (~1.57 eV), but also that this shoulder occurs at higher absorption coefficients than most other comparable semiconductors. This fact clarifies why very thin absorber films are sufficient for perovskite solar cell manufacture [15-16]. Moreover, due to the purely exponential trend of the Urbach tail, any traces of absorption by deep levels are observed below the absorption bandedge. This influences such high open-circuit voltage (V_{OC}) values [17] (up to 1.13 V) compared with their bandgap.

In the present study, we focus on the nature of the exciton recombination channels below/above the orthorhombic-tetragonal phase transition (165 K) depending on the crystalline-size of perovskite films to clarify the origin of the dual emission peak already observed at low temperature. Previously it has been verified in other kind of structures that periodicities of the order of 250 nm can produce duplication of bands [18]. To that end, we have studied the dependence of the emission and absorption properties of the perovskite-films on the grain-size using time-integrated, time-resolved photoluminescence (PL) spectroscopy and measuring the absorbance curves and the photocurrent on the cell. We have found that the grain-size is responsible of the appearance or disappearance of a dual emission on $CH_3NH_3PbI_3$ at low temperatures. A minimum size is required to observe both the unusual blueshift of the bandgap and the dual emission reported in perovskite materials [6]. Moreover, the dependence of photoluminescence spectra on temperature and excitation wavelengths was also determined. Our findings provide new insights into the photophysical processes occurring in perovskite films.

2.- METHODS AND MATERIALS

2.1.- Samples preparation and description

Samples preparations have been previously explained [19]. Fluorine-doped tin oxide (FTO) coated glass was carefully cleaned with ultra-pure water and ethanol. Then the substrates were dried using a N_2 stream. A ~ 40 nm thickness layer of TiO_2 was deposited on the FTO coated glass by spin-coating an anhydrous ethanol solution of titanium isopropoxide and heated at 500 °C for 30 min in room atmospheric conditions. On this TiO_2 buffer layer was deposited a 200 nm TiO_2 mesoporous layer. Halide perovskite $CH_3NH_3PbI_3$ 'cuboids-like' films of 350 nm (S1) and 300 nm (S2) thickness were deposited inside a glovebox by spin-coating 100 µL of perovskite precursor solution, 40% (w/w) dimethylformamide (DMF) solution of CH_3NH_3I and PbI_2 (3:1 molar ratio) at 4000 and 5700 rpm, respectively for 60 s. After the deposition, the substrate was kept at room temperature for 15 min and then heated up to 100 °C during 1 h inside an oven under air atmosphere. SEM images of the substrate were obtained using a JSM-7000F JEOL 216 FEG-SEM system using secondary and retrodispersed electron beams (Figure 1).

2.2.- Experimental Set-Up

Samples have been characterized by placing them in the cold finger of a commercial closed-cycle compressed helium cryostat (ARS DE-202). This cryogenerator has a heating resistance and a thermometer, with which the temperature can be controlled from 10 K to room temperature. The excitation/collection optics is placed out of the cryogenerator, because a near infrared (NIR) transparent window separates the cryogenerator from the optical setup. Filters are used to control the intensity of the excitation source (blue-laser). The diameter of the excitation area on the sample is approximately 3 microns. In the case of Time Resolved Photoluminescence (TRPL) experiments, the main optical axis is defined by the entrance slit of the Streak Camera. When measuring in continuous wavelength (CW) excitation conditions, light is redirected to a double 0.6 m focal length monochromator through a multimode optical fibre (200 µm core) adapted directly to the rail, and synchronously detected by a silicon avalanche photodiode (Si-APD) [20-21], a cooled germanium detector using the Lock-in technique or a Si Charged Coupled Device CCD, depending on the spectral response needs.

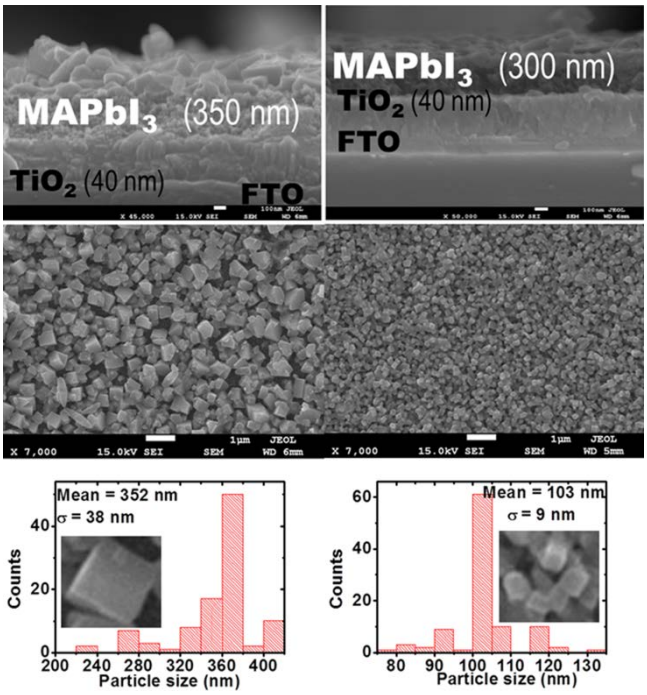

Figure 1.- **(From up to down)** Thickness of the perovskite samples, homogeneity in terms of their dimensions and particle sizes (Mean of the dimensions of the particles and their standard deviation, σ). The structural and morphological characterization was obtained by using a JSM-7000F JEOL 216 FEG-SEM system. (***Left***) particle size 352 nm. (***Right***) particle size 103 nm

3.- RESULTS AND DISCUSSION

In order to reach a deeper understanding of the underlying physical mechanisms of $CH_3NH_3PbI_3$ (hereafter $MAPbI_3$) films, we have investigated the crystalline-size dependence of optical absorption and photoluminescence emission. It has been previously seen that this is an important factor in absorption phenomena [22-23]. The accurate control of the crystalline size and shape of particles that constitute the perovskite films helped us to eliminate the random signals due to surface morphology of spatially inhomogeneous samples [12, 24-25]. Moreover, the dependence of photoluminescence spectra on temperature and excitation wavelengths was also determined.

3.1.- Optical absorption: The exciton binding energy and Eg in $MAPbI_3$

The evolution with temperature of the absorbance curves in small and large grain samples, that is to say, for grains of two different average sizes (352 and 103 nm, hereafter also denoted as S1 and S2, respectively) of $MAPbI_3$ were measured.

As shown in Figure 2, the material with larger grains transforms from the tetragonal into the orthorhombic phase at Tc = 150 K, and both phases undoubtedly coexist below Tc down to approximately 110 K (see inset Figure 2*a*) [26]. The absorbance spectra clearly show an excitonic absorbance resonance in both phases:

i) For the orthorhombic low-T phase, the exciton resonance is clearer and fairly narrower as temperature decreases (down to 7 K). It has a Lorentzian rather than Gaussian broadening.
ii) In the case of the tetragonal high-T phase, the excitonic resonance remains up to about 220 K, above this temperature being only observed as a shoulder (shallow maximum).

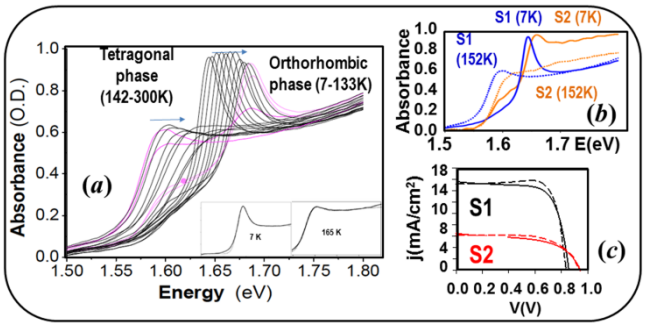

Figure 2.- (***a***) Evolution with temperature of the absorbance in larger $MAPbI_3$ grains. Transition phase around 150 K. **Inset:** Fitting using Elliot-Toyozawa theory with Lorentzian (low T region) and Gaussian (high T region) broadening. **(Left inset)** Orthorhombic phase at T = 7 K with an effective Rydberg energy of 23-25 meV. **(Right inset)** Tetragonal phase at T = 165 K with an effective Rydberg energy of 12-13 meV. (***b***) Normalized absorbance curves of larger and smaller -grain samples (denoted as S1 and S2, respectively) at two different temperatures, 7 K and 152 K (phase transition). S2 curves have been multiplied by a factor of 3 and 3.5 to be compared with curves of sample S1. (***c***) JV curves. Cell devices prepared in the same conditions that perovskites S1 and S2. Dashed line: from 1.2 V to -0.1 V. Continuous line: from -0.1 V to 1.2 V.

It must be noted that the low-energy part of the spectrum is purely excitonic, while the high-energy part also presents the continuous excitonic absorbance or band-band.

For the sake of comparison, Figure 2*b* shows the absorbance curves of the samples with different grain sizes at two temperatures, 7 and 152 K (temperature at which the orthorhombic to tetragonal transition occurs). The S2 curves have been normalized to be compared, multiplying by a factor of 3.5 for the low T phase and by a factor of 3 for high-T phase. Hence, the optical density at sample S2 is a factor 3-3.5 smaller than at sample S1, which is consistent with the difference in thickness and hence the corresponding smaller photocurrent measured on the cell (Figure 2*c*). It can be clearly seen that the excitonic front is somewhat wider and shifted towards high energy in the sample S2 (smaller grains) in relation to sample S1 (larger grains). This fact might be due to a confinement effect.

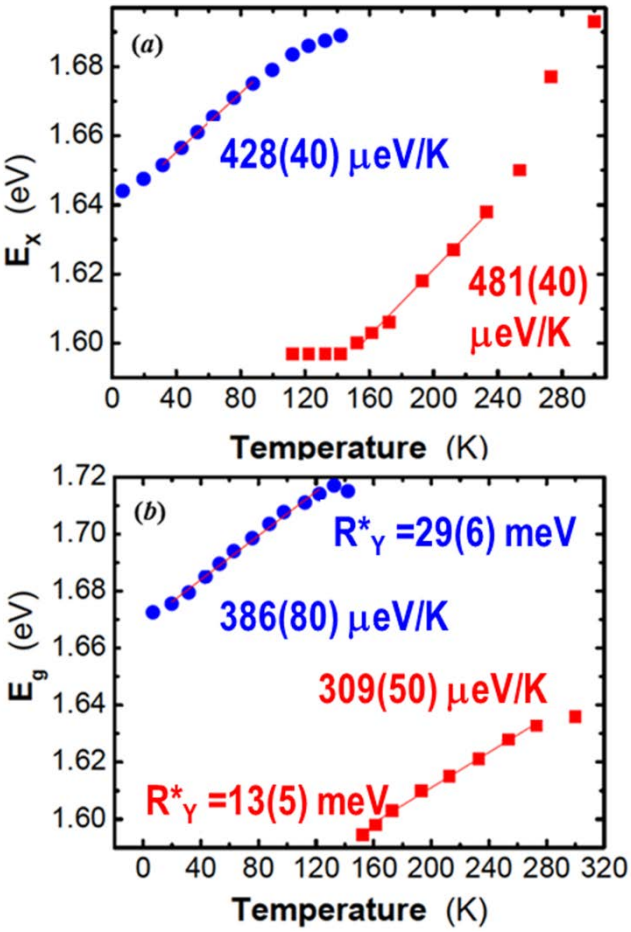

Figure 3.- (***a***) Excitonic binding energy in $MAPbI_3$. (***b***) The evolution of bandgap energy E_g (T).

Fitting the absorbance spectra using Elliot-Toyozawa theory with Lorentzian (low T region) and Gaussian (high T region) broadening it can be obtained (see Figure 3*a*) the evolution for the orthorhombic phase represented by blue circles; as well as, the evolution for the tetragonal phase represented by red squares, (the points between 240 K and 300 K are less precise since the maximum cannot be unequivocally distinguished). The shift of the excitonic peak with T has a positive rate (contrary to that observed in Si, Ge and III-V semiconductors and II-VI) of the order of 0.4-0.5 meV / K in both phases (see Figure 3*a* for exact fitted values). These values are very similar to those measured in PbS and PbSe semiconductors and hence due to Pb-orbitals contributing to the valence band of these materials. Figure 3*a* also confirms the decrease in the effective Rydberg energy of the exciton (approximately 10 meV reduction of the 1S exciton binding energy recently reported [27]). In old reports 35-50 meV were estimated from magneto-photoluminescence measurements [28-29].

After Toyozawa, Lorentzian/Gaussian broadening is related to weak/strong phonon coupling. Fitting of the full excitonic curves, we could also determine the dependence on T of the energy of the bandgap, Eg, for both phases (see Figure 3b). The observed variation is fairly linear and the values of the Eg-slopes are shown in the figure. The slopes are lower than those obtained for the excitonic binding energy, but similar to those observed in some IV-VI semiconductors.

3.2.- *Time-Integrated PL: Band studies*

Figure 4 shows the time-integrated PL spectra of a perovskite ($MAPbI_3$) film consisting of larger grains (average size 352 nm) at temperatures ranging from 15 K up to 293 K and using three different excitation fluences. As previously reported in literature, we observed two bands in the spectra and their behaviour can be described as follows:

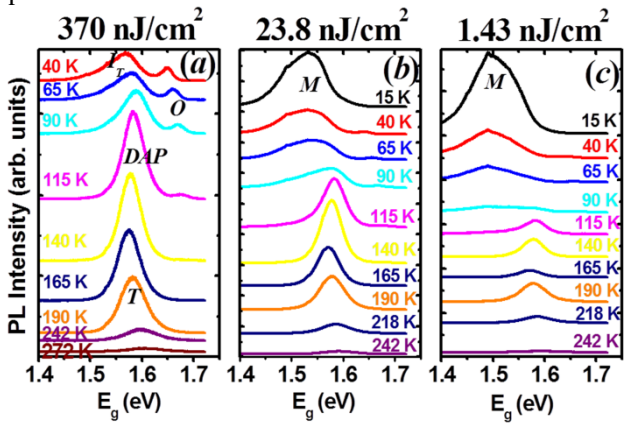

Figure 4.- Time-integrated temperature-dependent PL spectra of large-grains film of perovskite at three different excitation fluences: 370 nJ/cm² (***a***), 23.8 nJ/cm² (***b***), 1.43 nJ/cm² (***c***).

(i) Traditionally, the higher-energy band has been associated to the orthorhombic phase (O). This higher-energy emission peak 'O' can only be observed at high-fluence excitation (see Figure 4a) and it gradually appears below 140 K, although it is almost imperceptible throughout the whole low temperature range. This band is placed nearby the corresponding absorption onset [14]. According to the polaronic mechanism, the spectral width of this band does not decrease with temperature, leading to a characteristic and enduring finite line width, even at very low temperatures [30-31].

(ii) The low-energy band, on the other hand, has been associated to the tetragonal phase and at high-fluence excitation it is perceptible throughout the whole measured temperature range, even at low temperature range, causing the appearance of dual emission (see Figure 4). There is a remarkable predominance of the low energy PL band for T = 140K (23.8 nJ/cm²), as well as for the transition region at T = 115K (370 nJ/cm²). However, the shape of the PL emission in this tetragonal phase ('T') is independent of the fluence excitation excluding contributions of defect broadening. Some authors have assigned the lower energy band of this dual emission at high-fluence excitation: (i) to a donor-acceptor pair (DAP) around the transition [12], and (ii) to the inclusion of the tetragonal phase (I_T) at temperatures below the phase transition [13, 14, 26, 32]. Therefore, residual tetragonal $MAPbI_3$ crystals could coexist and be responsible of this dual-emission. One of the arguments in favour of the inclusion of the tetragonal phase at high-fluence excitation is that at temperatures below the phase transition we still detect emission centred on the similar energy as in the room-temperature phase [14]. Recently, it has been pointed the importance of the nature of the organic cation ($CH_3NH_3^+$) on the appearance of dual emission [6, 33], whereas the nature of the halide ion (I, Br) has been supposed to have negligible impact [6]. In other words, the atomic ordering in the organic cation takes place progressively when cooling down.

(iii) Lastly, the S1 sample at low-fluence excitation (see Figures 4 b and c) shows important differences with respect to the high-fluence excitation previously reported. We have measured a new sub-low energy band labelled 'M'. For the lowest excitation power used (1.43 nJ/cm²) there is a strong red shift at T < 115K of the 'M' band (see Figure 5); whereas the energy at which the 'T' and 'O' emissions are centred does almost not change with decreasing fluence-excitation. Moreover, there also exists a strong red shift with decreasing power, the detected emission of 'M' being no longer centred on similar energy as the room-temperature 'T' phase. Therefore, the bandgap energy strongly depends on the fluence-excitation on this region.

Moreover, below 45 K, this sub-low energy band labelled 'M' seems to change its tendency and present a blue-shift with decreasing temperature. Thus, the behaviour of this sub-low energy band, which does not appear in the small grain perovskite film and reaches the maximum in PL intensity at the temperature of 15K for the power of 1.43 nJ/cm², might be explained as bound–state excitons [10] rather than an inclusion of the tetragonal phase.

Hence, a more detailed study of the grain structure should be carried out to gain deeper insight into the dependence on the crystalline-size of the fundamental properties and processes taking place in this perovskite.

Figure 5 shows the energy values of the bands as a function of temperature obtained from the PL spectra. By decreasing the temperature, the bandgap energy of the tetragonal band decreases linearly until T = 165 K. Table 1 summarizes the values of the temperature coefficient $\alpha = \partial E/\partial T$ obtained for different fluences-excitations. Moreover, the comparison between the calculated [34] and measured energy bandgaps of $MAPbI_3$ is collected on Table 2. By decreasing the temperature between 165K > T > 115K, it exists a transition region before arriving to the orthorhombic structure. Below the tetragonal-to-orthorhombic phase transition, there is a strong dependence of the PL spectra on the excitation-fluence, as shown in Figure 4. As the excitation-power is decreased, the intensity of the lower-energy band remarkably drops, broadens and shifts to lower energy while the higher-

energy band nearly vanishes (see Figure 4). Due to the fact that it has been already observed two coexisting crystallographic phases [35-37] in several inorganic perovskite materials of mixed [38-40] and pure [41-43] composition, including $MAPbI_3$, we suggest that the measured emission in the low-temperature phase could be explained by supposing a very small relative volume fraction of low-energy sites attributable to small embodiments of individual tetragonal-phase crystallites, where photoexcited carriers can be trapped [14]. Therefore, the sub-gap sites in the tetragonal crystallites can only be partially filled under weak excitation by the few free carriers. On the other hand, the emission observed at higher energy under strong excitation could be caused by the remained carriers in the orthorhombic phase after saturating the tetragonal crystallites. Moreover, others arguments in favour of the inclusion of the tetragonal phase at high-fluence excitation are that: (i) at temperatures below the phase transition we still detect emission centred on the similar energy as in the room-temperature phase [14], in contrast to the increase in bandgap energy measured by optical absorption (see Figure 2). (ii) The shape of the tetragonal band endures almost unaffected at temperatures above the phase transition; however the spectral width decreases from 300 K till 140 K. This is in line with a smaller available phonon population. (iii) The phonon coupling effects could also explain the relatively large width of the tetragonal band [44]. Nevertheless, we have to keep in mind that these hypotheses are not theoretically verified [6] and could be unsatisfactory to describe the whole complex phenomenology attached to these perovskite materials. For example, Dar et al. argued that although $CH_3NH_3PbBr_3$ presents dual emission at room temperature, it is not possible the existence of tetragonal inclusions in the cubic phase [6]. Hence, it is still required not only an explanation that take account all the observed trends of the PL spectra over the whole temperature range (15 to 300 K) [6], but also new experiments that allow to identify new dependences in perovskite materials.

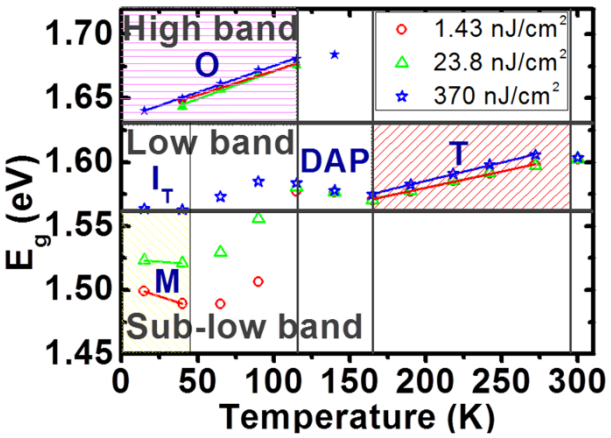

Figure 5.- Temperature dependent data of the bandgap energy of the three bands obtained from the PL spectra. The sample is the larger grain (352 nm) perovskite film (thickness 350 nm). The uncertainty of the data is less than the size of the symbol.

In order to confirm the possible physical mechanism for the low-temperature emission of the $CH_3NH_3PbI_3$ large-grain film, we plot in Figure 6 (a-c) the emission normalized to the higher energy band (orthorhombic phase) at 40K (for 352 nm thick-grain film), at 50K (for 103 nm thick-grain film), and at 50K (for <80 nm thick-grain film), respectively. From comparison to the excitation spectra (Figure 2a) at this temperature, it can be inferred that photoexcitation takes place entirely through the bandgap of the orthorhombic phase (at about 1.69 eV), even though the dominant emission is related to the bandgap of the tetragonal phase (at about 1.60 eV). That is because quantifiable excitation through this transition at about 1.6 eV is not possible as the comparison of the emission and excitation spectrum suggests [14]. This implies that, despite the small relative volume fraction of low-energy states, these sites offer the predominant radiative exciton-recombination-pathway [14]. From comparison of emission and excitation spectra it can be deduced that small individual crystallites could cause at the phase boundaries a high density of sub-gap states. In fact, we can infer from Figure 6 that the grain size determines which band has more weight for a fixed high-power. Thus, increasing the grain from 80 nm to 352 nm, it is possible to enhance the tetragonal band versus the orthorhombic band. Indeed, for grain sizes greater than 352 nm, we would be able to eliminate the orthorhombic band. At the same time, a grain size of 100 nm is the optimum size to obtain the same weight in both bands (for a high power). This dependence on grain size of the structure-stability has been already observed in others materials [45]. Hence, although traditionally the temperature of 165K had been associated as the tetragonal-to-orthorhombic phase transition temperature, we can see in Figure 6 that the increase in grain size allows slowing down the phase transition. On the other hand, the thickness of the perovskite layer has no influence in the appearance or disappearance of the dual emission. However, the thickness of the layer is a much more important factor than the size of the grains in the location of the energy of the bandgap (see Figure 6).

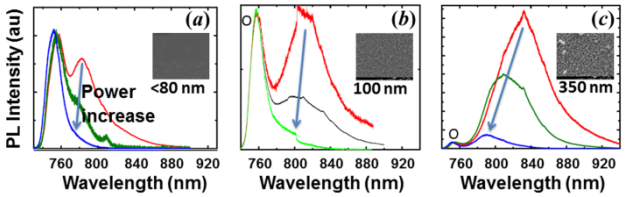

Figure 6.- PL intensity depending on the wavelength for three different powers and for a temperature of 40-50 K, well below the phase transition temperature. It corresponds to the sample of a 600 nm (***a***), 350 nm (***b***), and 300 nm (***c***) thick continuous $CH_3NH_3PbI_3$ 'cuboids-like' film. The grain-sizes are <80 nm (***a***), 103 nm (***b***), and 352 nm (***c***), respectively. The PL Intensity was normalized at the higher-energy band. Inset: SEM images of the three spatially homogeneous and conformal films of $CH_3NH_3PbI_3$ perovskite with corresponding crystal sizes.

3.3.- Deconvoluted Gaussian fitting

3.3.1.- Bandgap Energy

A fundamental key to improving the conversion efficiency is to better understand the yet unclear exciton-recombination-pathways [46]. For this reason, and due to the still existing contradictions when trying to interpret the PL emissions, a detailed Gaussian fitting deconvolution is necessary. This can help to give insight not only into the origin of the dual emission peak, but also into the existence or not of phonon-assisted indirect transitions causing the tetragonal emission. It has been observed that the intensity of the orthorhombic band decreases with increasing temperature, while the intensity of the tetragonal band progressively increases. Some authors have interpreted that the PL tetragonal-band emission stems from phonon-assisted indirect transitions during the exciton recombination process, whereas the PL orthorhombic-band emission is originated from direct transitions [47]. Other authors, however, defend that the PL emission of the tetragonal band, which is observable for the entire temperature range, cannot be ascribed to the indirect bandgap emission affected by a quantum confinement effect [48]. In this context, the thorough deconvolution of our time-integrated temperature-dependent PL bands into Gaussian peaks could provide information on the exact number PL emissions of $CH_3NH_3PbI_3$ perovskite films and their characteristics, and allow to correctly interpret them.

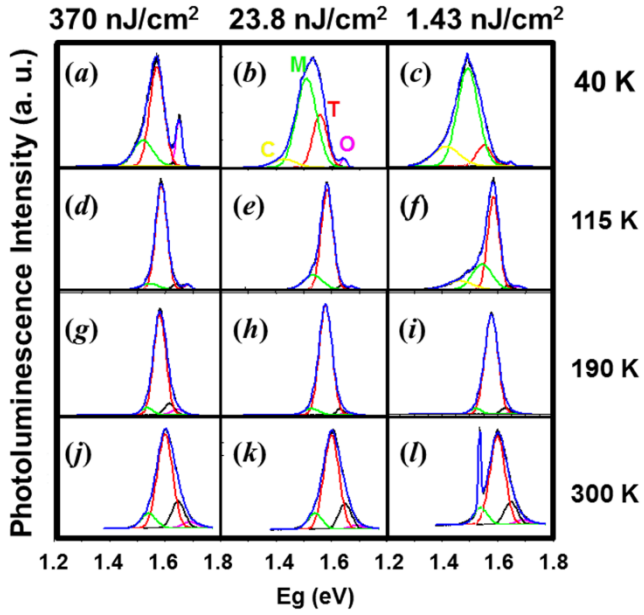

Figure 7.- Deconvoluted time-integrated PL spectra profiles for the large-grains film by using Gaussian fitting. Each row shows the profiles, depending on the power, at a given temperature associated with each of the four different phases of the perovskite. Peaks assignment: pink (orthorhombic), red (tetragonal), green (monoclinic), yellow (cubic).

Keeping that in mind, we have deconvoluted the measured time-integrated PL spectra profiles by using a Gaussian fitting as shown in Figure 7. Only spectra at a few selected temperatures for each fluence are shown. The typical PL profile for the large-grains film can be divided into several Gaussian peaks, as illustrated in Figure 7. The different colours used for each of the deconvolution peaks are associated with the different symmetries defining the perovskite structures (see Figure 7 caption). Therefore, for high fluence and temperatures below 115 K, we can asseverate that the tetragonal and orthorhombic phases coexist (Figure 7*a*). This structure coexistence scenario clarifies the presence of the tetragonal peak throughout the complete temperature range studied (15–300 K). Alternatively, this tetragonal-orthorhombic coexistence might correspondingly be a consequence of transitions between different points on the Fermi surface [26].

To analyse and understand the meaning of the different peaks, we make use of Figure 8, where all the values for the bandgap energy and Full Width at Half Maximum (FWHM) are plotted. From Figure 8*a* it can be seen that there are three different temperatures for which the FWHM changes its tendency (45.5K, 165 K, 300 - 272 K). Some of these temperatures have been already associated with phase transitions previously reported in literature. For example, Weller et al. [49] explored the complete structure of $MAPbI_3$ by using neutron powder diffraction for the temperature range between 100 and 352 K, which has yield key evidences on light atom locations in this heavy metal compound [49]. Thus, 300 - 272 K corresponds to the phase transition from cubic to tetragonal [49], whereas 165 K corresponds to the transition of phases from tetragonal to orthorhombic [49]. Hence, it can be deduced that 45.5 K could also be associated with a new structural transformation/phase transition. That is to say, the temperature dependence of the peak positions and widths suggests the existence of a novel phase below 45.4 K, which has not been previously reported in literature. Hence, the existence of this possible new polymorph remains to be proven. Others arguments in favour of our observation are that: (i) The structural systematics in the isostructural compound at room conditions $MAGeCl_3$ evidence the existence of four different phases: cubic, trigonal, orthorhombic and monoclinic going down in temperature; (ii) It is known that the $\{PbI_3\}^-$ framework becomes less distorted with the raise of temperature, while the MA^+ cation experiences larger atomic translations and displaces leisurely to the centre of the perovskite cube, taking place the creation of the cubic phase at 327 K [49]. The freely rotating MA^+ cation on the picosecond timescale (typical of the cubic structure) is progressively detained by decreasing the temperature. Hence, for the tetragonal structure, exists only eight disordered MA^+ states [49, 50], whereas in the orthorhombic (Pnma) structure the cations are fixed. Quarti et al. [51] explored stable MA^+ cation orientation reachable within 0.1 eV per unit cell by using polar and apolar structural models. This study showed a variety of stable structures. This fact supports the existence of domains with different orientations prevailing within the same crystal [49, 51].

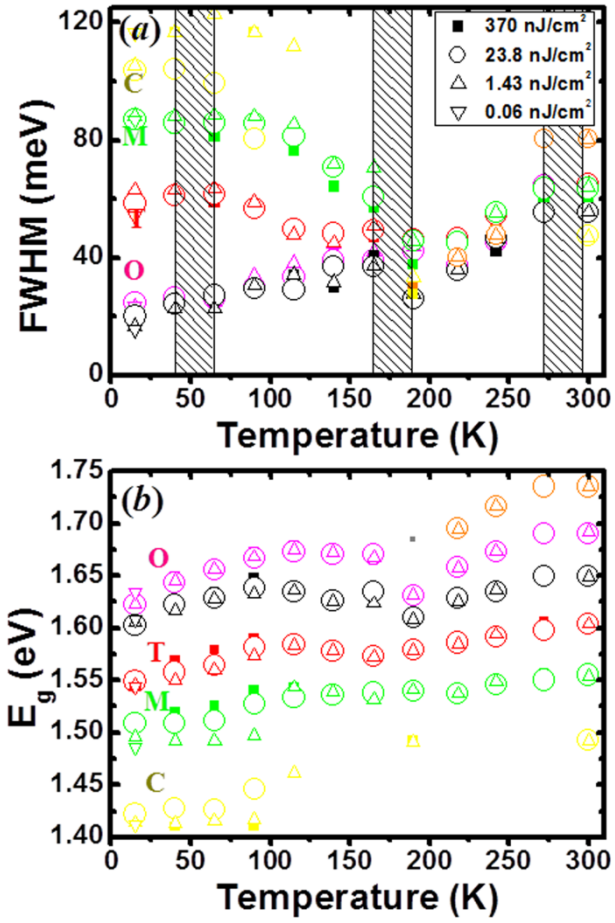

Figure 8.- Temperature dependent data of (***a***) the full width at half maximum and (***b***) the bandgap energy of the different peaks obtained from the PL spectra by using deconvoluted Gaussian fitting. Note that the orthorhombic structure has a larger bandgap than the tetragonal structure, as theoretical calculations have already revealed [27]. The uncertainty of the data is less than the size of the symbol.

Keeping this in mind, we suggest that, by decreasing the temperature, an extra symmetry lowering takes place leading to the new-phase. This new-structure, which forms around 45.5K, should be identifiable from X ray-diffraction, but probably difficult to determine due to the existence of multiple twin domains. Hence, the existence of the latter low-symmetry for T < 45.5 K cannot be discarded. Moreover, our results suggest that PL is as a suitable method to explore the structural phase transitions in organometal-halide perovskites.

At this point, we will analyse the evolution of the linewidth (FWHM; Γ) with the temperature (see Figure 8*a*), keeping in mind that the independent Boson model is no longer valid [52]: *(i)* At low temperatures (T < 45.5 K) we would obtain the inhomogeneous broadening contribution (Γ_o =74.4 meV). This term dominates at relatively low temperatures, and a nearly constant broadening was expected. This result is larger than the obtained in a less precise way where it was obtained a value of 38 meV [26], while it is much more similar to the behaviour described more recently by Dar et al. [6]; *(ii)* While raising the temperature from 45.5 to 165-218 K, it was found that the linewidth decreases (increases) almost linearly with temperature for the C-, M-, T-, peaks (O- N- peaks). At this point, it is expected that acoustic (σ) and optical phonon (Γ_{op}) contributions dominate. The maximum value of both contributions to width broadening corresponds to 70 meV, and varies between $\sigma + \Gamma_{op}$ = 70 – 40.4 meV depending on temperature; *(iii)* At temperatures above 165-218 K, an increase of the linewidth with temperature is measured. The contribution to width broadening from the acoustic phonons can be neglected [26], and the optical phonon energy takes a value of Γ_{op} = 27.0 meV. This outcome is consistent with a Raman scattering experiment on $CH_3NH_3PbI_3$, which revealed optical phonons with an energy of 25–42 meV for the torsion mode of the organic cations, whereas the vibration of the inorganic cage and the libration of the organic cations are associated with much smaller energies [26].

Moreover, it can be demonstrated that the shift of the linewidth (ΔFWHM) scales with the FWHM, although this dependence varies in each one of these three already exposed regions. It is necessary to note, that Γ_o = 74.4 meV is the inflection value that causes the linewidth to decrease or increase with temperature. For a linewidth < 74.4 meV (> 74.4 meV), the linewidth will increase (decrease) with increasing temperature. This variation will be larger as we move away from $FWHM_o$.

As shown in Figure 5, when studying the bandgap energy we have distinguished three blocks (high, low and sub-low). Further in-depth analyses of the PL spectra reveal that they can be better described by 5-6 peaks, as obtained from Gaussian fit deconvolution (Figure 8b and Table 2). These peaks will be here labelled Orthorhombic, Tetragonal, Monoclinic, and Cubic, from higher to lower energies and shown in Figure 8b. All these peaks behave similarly during heating up. Both the lower-energy emission peak attributable to the tetragonal phase (T) and the highest-energy emission peak attributable to the orthorhombic phase (O) of $CH_3NH_3PbI_3$ experience two-times the blue-shift previously reported [6]. Additionally, a continuous blue-shift for temperatures higher than 165 K has been also observed. Both blue-shifts can be described by a temperature coefficient $\alpha = \partial E/\partial T$ (see Table 3). Wu et al. [26] gave only the value of α for the tetragonal structure (and for high temperature) of 0.30 meV/K, which it is similar to that obtained by us (0.268 meV/K). Additionally, we have obtained α for all the different peaks and they define three clear temperature regimes: (i) blue-shift between 45.5 and 115 K, (ii) red-shift between 115 and 165 K, and (iii) another blue shift between 165 K and 272 K. Hence, while raising the temperature from 115 to 165 K, the whole of the peaks reveal a systematic redshift, whereas an unusual blueshift is observed for temperature higher than 165 K. The blue-shift between 165 K and 272 K is probably connected with the opposite effects on the bandgap energy of the relationship between the thermal expansion and the electron–phonon renormalization [26], as occur in IV-VI semiconductors (PbS, PbSe, PbTe, for example) [53]. It has been already reported its disagreement

with the empirical Varshni [54] Pässler [55] and Bose-Einstein [56] models of standard tetrahedral semiconductor. However, so far, this blueshift behaviour has also been measured in no conventional semiconductors, such as lead/copper chalcogenide semiconductors [57]. Furthermore, it can be demonstrated that the blue-/red-shift (ΔEg) scales linearly with the Eg. Thus, we obtain that the value of the fundamental perovskite bangap is Eg_o (45.5K) = 1.38 eV, which is the ideal value for single-junction photovoltaic applications. Thus, $CH_3NH_3PbI_3$ is found to possess a direct bandgap of 1.38 eV. Moreover, fundamental perovskite bangap energies (Eg_o) at 165 and 300 K are 1.47 and 1.44 eV respectively.

3.3.2.- *Binding Energy*

Much has been conjectured about the great disparity of the estimated values of binding energy E_B. To clarify this point, in Figure 9 we have represented the peaks integrated intensities as a function of 1/T. Two distinct behaviours are observed. The tetragonal-orthorhombic transition-temperature separates both regimes. Moreover, minimum values of the integrated intensity are obtained at T = 45 K, 165 K, and 280 K. To fit this temperature-dependent Free Exciton emission intensity, we have used the following equation [58, 59]

$$I\,(T) = \frac{I_0}{1 + Ae^{-E_B/k_BT}}$$

in which I_o is the intensity at 0 K, and k_B the Boltzmann constant.

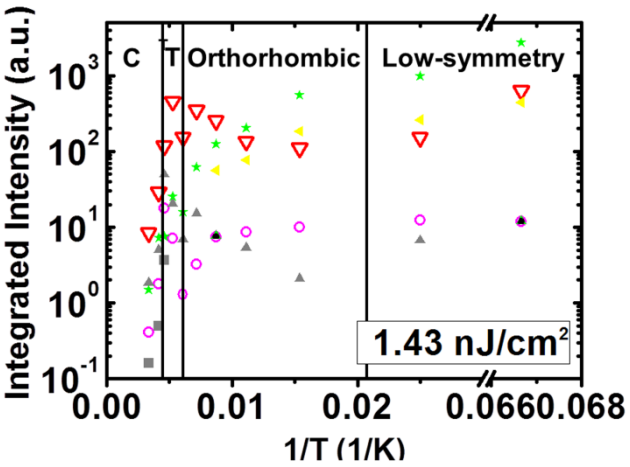

Figure 9.- Temperature dependent data of integrated intensity at the laser excitation power of 1.43 nJ/cm² . Phase transitions are associated with local minima. The uncertainty of the data is less than the size of the symbol.

First of all we made the fitting obviating the difference of behaviour before and after the transition-temperature. In this case we have represented the values obtained for the E_B in Table 4. In that way, we have estimated the fluence-dependence of E_B for three of these peaks: tetragonal-, orthorhombic-, and low-symmetry- structure. Thus, an increase in E_B is observed with the decrease in power. The values obtained for the orthorhombic phase are concentrated between 42 meV (370 nJ/cm²) and 56 meV (1.43 nJ/cm²), whereas for the tetragonal phase they vary between 25 meV (370 nJ/cm²) and 61 meV (1.43 nJ/cm²). The highest values obtained for the tetragonal phase are close to those published by some authors. For example, for the $CH_3NH_3PbI_3$ film, it has been published E_B values of 62. 3 meV from PL measurements [26] and 55 meV from the absorption data [26] or 50 meV from the magneto-absorption data [60]. Nevertheless, we should note that this exciton binding energy was obtained without taken into account the two different behaviours before and after the transition-temperatures, therefore this exciton binding energy may be overestimated, being the upper bound for E_B of halide perovskites.

It would be more accurate to differentiate for temperatures lower and higher than the transition-temperature. Thus, for the tetragonal structure are obtained lower exciton binding energy values (see Table 4). This values agree with the 18–24 meV [27] or the 32 meV [14, 59] already reported for the tetragonal structure by using microwave photo-conductance and PL study. This study suggests that for the same composition, the exciton properties of hybrid perovskites are sensitive to the fluence, temperature, synthesis and structure details, such as grain-size. As it has been probed, at high temperature, the exciton screening (due to collective orientational motion of the MA^+ cations) produces a large population of free carriers [27].

3.3.3.- *Excitonic character of the peaks*

The fluence-PL dependence was additionally conducted in the range of 0.06~370 nJ/cm². The position and intensity of the different PL bands/peaks vary also with laser fluences, because of the inherent bandgap of the $MAPbI_3$ increases with the accumulation of charges during photo-excitation [6, 61]. With increasing fluence at temperature below 90K, it is observed a continuous blue shift of the low-energy emission band (tetragonal- and low-symmetry -phase), due to the tetragonal band filling effect [61]. Deconvolution shows how the tetragonal peak fills with fluence-excitation; whereas the low-symmetry peak 'M' decreases (see Figure 7 a-c), causing the blue shift of the low-energy emission band. Indeed, once the tetragonal peak has been filled, it is when the orthorhombic peak begins to increase. At high-fluence, the coexistence of the tetragonal phase and the orthorhombic phase is observed. Figure 8b shows as the different peaks undergo a blue-shift with the fluence-increase, being greater for the peaks assigned to smaller Eg. In contrast, only at higher fluences (>200 nJ/cm²) it is when the orthorhombic peak could show a blue shift. This could be explained if the dynamic charge transfer from the orthorhombic-to-tetragonal structure takes place at lower fluences (<200 nJ/cm²). Hence, the band filling effect dominates at higher fluences (>200 nJ/cm²).

At temperature lower than 45.5 K, a perceptible sub-linear dependence of the integrated PL intensity on the fluence was detected in the Eg position of the 'C' peak obtained by deconvolution; whereas the low-symmetry peak 'M' was almost lineal (see Figure 10). This sub-linear depend-

ence observed for T < 40K can be produced by the inefficient diffusion of the photogenerated carriers, and suggests the presence of non radiative recombination at low temperature (see Figure 11). In contrast, the rest of the peaks display an overlinear relationship between the fluence and the integrated PL intensity. At higher temperatures, the 'C' peak disappears; whereas the rest of the peaks go closer to a biexcitonic behaviours as shown in Figure 10. An increment in the carrier density yields the saturation of non radiative recombination centres, getting better effective internal quantum efficiency, and suggesting that Auger recombination plays a minimal role under this fluence [6].

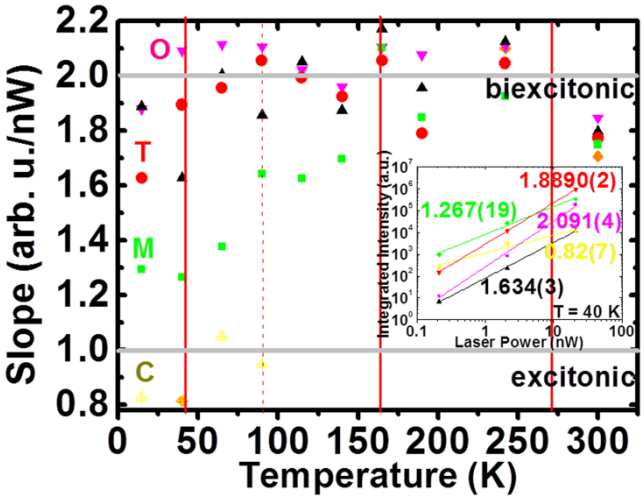

Figure 10.- Excitonic character of the peaks: Cubic (exciton, X), tetragonal (biexciton, 2X), low-symmetry 'M' (trion +, X^+), and orthorhombic ($2X^+$) peak. Inset: Excitation fluencies dependent data of integrated intensity at the temperature of 40 K. That was used to determine each of the values of the slopes plotted in Figure 10.

From Figure 10 can be also deduced that one C-exciton ('C' peak) exists in our larger-grain perovskite film. On one side, it could think that the spin-orbit splitting of the valence band could produce anothers different excitons, M-exciton (low-symmetry peak 'M'). Because of Figure 8b, in which the optical gap for C-exciton is smaller, the hole of the C-exciton (M-exciton) should be situated in the upper (lower) branch of the Valence band. However, this M-exciton (low-symmetry peak 'M') also could be understood as a positive trion, in which the exciton bounds to a hole. In our PL spectrum of Figure 7(b,c), can be observed the existence of a low-symmetry 'M' (trion, X^+) peak stronger than the 'C' (exciton, X) and the tetragonal (biexciton, 2X) peak (see Figure 10) . This could be a signature of an extrinsic doped monolayer, arising from charged trap states present in the SiO_2substrate. The Orthorhombic phase, which has been detected at higher temperature and excitation fluencie, is associated to a $2X^+$.

3.4.- Time-Resolved PL

It has been also measured the time-resolved photoluminescence emission by mean of time-correlated single photon counting at different temperatures, excitation fluencies and emission energies. From these measurements it has been calculated the lifetime that can be seen in Figure 11. At an excitation fluencie of 370 nJ/cm² (see Figure 11), it has been calculated the radiative emission of the lower energy band (red line/circle) and the higher energy band (orthorhombic peak, purple line/square). The radiative emission shows clearly three drops of the lifetime with the temperature, which confirm the temperatures of the three phase transitions already determined by time integrated PL. In addition, there is a concordance with the temperatures at which the minimum values are observed in the integrated intensity versus 1/T of Figure 9. From Figure 11, it can be also seen that in all the phase-transitions (at 165 K and around 280 K) only the radiative emission takes place; with the exception of the transition that takes place at the temperature close to 45.5 K (in which both the radiative and non-radiative emission are involved, as it was suggested from Figure 10). As aforementioned, our results suggest that a phase transition from a low-symmetry to an orthorhombic phase occurs at that temperature where the symmetry of the anionic sublattice is modified, whereas no ostensible modification of the cation dynamics is suggested. By using a three-level model with thermal activation energies (E_{act}) of 53.63, 45.67, and 50.86 meV, depending on the PL components, we can explain a possible non-radiative emission at 45.5 K by PL quenching due to thermal escape of electrons. This would explain why when increasing the temperature to 140 K there is a decrease in the intensity of the peaks associated with $2X^+$ (orthorhombic) and X^+ (monoclinic / rhombohedral) versus the increase observed for 2X (tetragonal) (see Figure 7). Additionally, dark states of photo-excited carriers are revealed with the activation energies due to thermal excitation (E_{low}) of 41, 30.5 and 35.06 meV. In contrast, these activation energies are too low if we compared it to the onset of the reorientation of the pyramidal $GeCl_3^-$ anion (627 meV) [62]; and no electron tunneling is observed. Thus, observing inset Figure 11 it is clear that halogen (I) shifts with the decrease in temperature while metals do not (Pb). This may remind the previously exposed ideas of displacements of anions (O_2) against the stillness of metals by applying high pressures to certain oxides. In this way, it could be difficult to recognize a phase transition by X-rays when looking at the positions of the metals (Pb) if they do not suffer appreciable displacements. Other techniques, such as Raman that, are sensitive to the vibrations of oxygen (halogens); or transient PL measurements can give us information of possible phase transformations that take place. In that way, we could discriminate between defects and phase transitions. Therefore, it is necessary to note that contrary to what has been argued [6], the importance of the halide ion (I, Br) should not be underestimated.

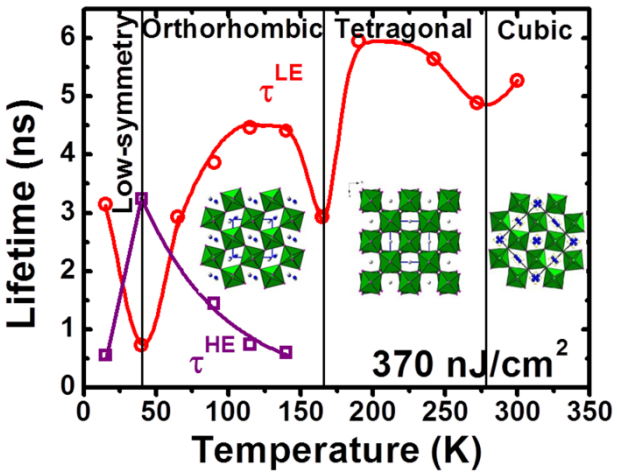

Figure 11.- Radiative lower-energy (τ^{LE}) and higher-energy (τ^{HE}) lifetime versus temperature for the excitation fluencies of 370 nJ/cm². Inset: Structural stability of $CH_3NH_3PbI_3$ as a function of temperature. The uncertainty of the data is less than the size of the symbol.

CONCLUSIONS

We have reported the optical absorption and photoluminesce emission characteristics of $CH_3NH_3PbI_3$ perovskite as a function of several important parameters such as grain-size, temperature, excitation fluencies wavelength and time (in the case of time-resolved PL measurements). This systematics and detailed study allows us clarifying the nature of the not well-known dual emission peak, finding absorption and emission tendencies and suggesting the existence of a novel low-temperature phase with symmetry reduction. Sometimes, for convenience, it can be assumed that the vibration of each group of bands is independent of the rest of the molecule or compound, but we should bear in mind that those vibrations can be strongly coupled. This fact makes techniques such as Raman and IR spectroscopies or transient PL measurements suitable sources of information of the atomic local environment and therefore sensitive to structural phase transitions. Thus, for instance, time-resolved PL emission data collected in Figure 11 evidence a phase transition for this $CH_3NH_3PbI_3$ compound at temperature close to 45 K. (More other evidences are given along the manuscript). X-Ray diffraction measurements, which provide the average structure of the sampled compound, are limited for systems such as that of this perovskite since the fixing of the atomic coordinates of the light elements of the cation are the responsible of the symmetry lowering at low temperatures. This reduction of symmetry below 45 K would also explain the increase of the number of bands.

AUTHOR INFORMATION

Corresponding Author

* raquel.chulia@uv.es

Author Contributions

All authors have given approval to the final version of the manuscript.

ACKNOWLEDGMENT

This work has received funding from the European Union's Horizon 2020 research and innovation programme under the Marie Sklodowska-Curie grant agreement Nº 704998 (RCJ). Financial support by the Ministerio de Economía y Competitividad (MINECO) from Spain under project, MAT2013-47192-C3-1-R (NASCENT) is also acknowledged.

REFERENCES

1. Dawson, J. A.; Naylor, A. J.; Eames, C.; Roberts, M.; Zhang, W.; Snaith, H. J.; Bruce, P. G.; Islam, M. S., Mechanisms of lithium intercalation and conversion processes in organic–inorganic halide perovskites. *ACS Energy Lett.* **2017,** *2*, 1818–1824.

2. Grivas, C.; Pollnau, M., Organic solid-state integrated amplifiers and lasers. *Laser Photonics Rev.* **2012,** *6*, 419-462.

3. Kagan, C. R.; Mitzi, D. B.; Dimitrakopoulos, C. D., Organic-inorganic hybrid materials as semiconducting channels in thin-film field-effect transistors. *Science* **1999,** *286*, 945–947.

4. Stranks, S. D.; Snaith, H. J., Metal-halide perovskites for photovoltaic and light-emitting devices. *Nat. Nanotechnol.* **2015,** *10*, 391-402.

5. Vicente, N.; Garcia-Belmonte, G., Methylammonium lead bromide perovskite battery anodes reversibly host high li-ion concentrations. *J. Phys. Chem. Lett.* **2017,** *8*, 1371–1374.

6. Dar, M. I.; Jacopin, G.; Meloni, S.; Mattoni, A.; Arora, N.; Boziki, A.; Zakeeruddin, S. M.; Rothlisberger, U.; Grätzel, M., Origin of unusual bandgap shift and dual emission in organic-inorganic lead halide perovskites. *Sci. Adv.* **2016,** *2*, 1601156.

7. Xing, G.; Mathews, N.; Sun, S.; Lim, S. S.; Lam, Y. M.; Graetzel, M.; Mhaisalkar, S.; Sum, T. C., Long-range balance electron- and hole-transport lengths in organic-inorganic $CH_3NH_3PbI_3$. *Science* **2013,** *342*, 344-347.

8. Stranks, S. D.; Eperon, G. E.; Grancini, G.; Menelaou, C.; Alcocer, M. J. P.; Leijtens, T.; Herz, L. M.; Petrozza, A.; Snaith, H. J., Electron-hole diffusion lengths exceeding 1 micrometer in an organometal trihalide perovskite absorber. *Science* **2013,** *342*, 341-344.

9. Huang, W.; Yue, S.; Liu, Y.; Zhu, L.; Jin, P.; Wu, Q.; Zhang, Y.; Chen, Y.; Liu, K.; Liang, P.; Qu, S.; Wang, Z.; Chen, Y., Observation of unusual optical band structure of $CH_3NH_3PbI_3$ perovskite single crystal. *ACS Photonics* **2018,** *5*, 1583–1590.

10. Xing, G.; Mathews, N.; Lim, S. S.; Yantara, N.; Liu, M.; Sabba, D.; Grätzel, M.; Mhaisalkar, S.; Sum, T. C., Low-temperature solution-processed wavelength-tunable perovskites for lasing. *Nat. Mater.* **2014,** *13*, 476-80.

11. Fang, H.-H.; Raissa, R.; Abdu-Aguye, M.; Adjokatse, S.; Blake, G. R.; Even, J.; Loi, M. A., Photophysics of organic-inorganic hybrid lead iodide perovskite single crystals. *Adv. Funct. Mater* **2015,** *25*, 2378-2385.

12. Kong, W.; Ye, Z.; Qi, Z.; Zhang, B.; Wang, M.; Rahimi-Iman, A.; Wu, H., Characterization of an abnormal photoluminescence behavior of perovskite $CH_3NH_3PbI_3$. *Phys. Chem. Chem. Phys* **2015,** *17*, 16405.

13. Panzer, F.; Baderschneider, S.; Gujar, T. P.; Unger, T.; Bagnich, S.; Jakoby, M.; Bässler, H.; Hüttner, S.; Köhler, J.; Moos, R.; Thelakkat, M.; Hildner, R.; Köhler, A., Reversible laser induced amplified spontaneous emission from coexisting tetragonal and orthorhombic phases in hybrid lead halide perovskites. . *Adv. Opt. Mater.* **2016,** *4*, 917–928.

14. Wehrenfennig, C.; Liu, M.; Snaith, H. J.; Johnston, M. B.; Herza, L. M., Charge carrier recombination channels in the low-temperature phase of organic-inorganic lead halide perovskite thin films. *Apl Materials* **2014,** *2*, 081513.
15. Yang, W. S.; Noh, J. H.; Jeon, N. J.; Kim, Y. C.; Ryu, S.; Seo, J.; Seok, S. I., High-performance photovoltaic perovskite layers fabricated through intramolecular exchange. *Science* **2015,** *348*, 1234–1237.
16. Wolf, S. D.; Holovsky, J.; Moon, S.-J.; Löper, P.; Niesen, B.; Ledinsky, M.; Haug, F.-J.; Yum, J.-H.; Ballif, C., Organometallic halide perovskites: Sharp optical absorption edge and its relation to photovoltaic performance. *J. Phys. Chem. Lett.* **2014,** *5*, 1035–1039.
17. Lee, M. M.; Teuscher, J.; Miyasaka, T.; Murakami, T. N.; Snaith, H. J., Efficient hybrid solar cells based on meso-superstructured organometal halide perovskites. *Science* **2012,** *338*, 643–647.
18. Chulia-Jordan, R.; Santamaria-Perez, D., Four-mode plasmonic structure based on a prism-grating anticrossing bandgap. *Appl. Phys. Lett.* **2012,** *100*, 063301.
19. Suárez, I.; Juárez-Pérez, E. J.; Bisquert, J.; Mora-Seró, I.; Martínez-Pastor, J. P., Polymer/perovskite amplifying waveguides for active hybrid silicon photonics. *Advanced Materials* **2015**, 6157-6162.
20. Muñoz-Matutano, G.; Barrera, D.; Fernández-Pousa, C. R.; Chulia-Jordan, R.; Martínez-Pastor, J.; Gasulla, I.; Seravalli, L.; Trevisi, G.; Frigeri, P.; Sales, S., Parallel recording of single quantum dot optical emission using multicore fibers. *IEEE Photonics Technology Letters* **2016,** *28*, 1257.
21. Muñoz-Matutano, G.; Barrera, D.; Fernández-Pousa, C. R.; Chulia-Jordan, R.; Seravalli, L.; Trevisi, G.; Frigeri, P.; Sales, S.; Martínez-Pastor, J., All-optical fiber hanbury brown & twiss interferometer to study 1300 nm single photon emission of a metamorphic InAs quantum dot. *Scientific Reports* **2016,** *6*, 27214.
22. Chulia-Jordan, R.; Unger, A., Comparison of the different bandgap cavities in a metallic four-mode plasmonic structure. *Plasmonics* **2015,** *10*, 429–438.
23. Chulia-Jordan, R.; Santamaria-Perez, D., Tuning the propagation constant by the anticrossing bandgap prism coupling technique. *Plasmonics* **2012,** *7*, 665–675.
24. Kao, T. S.; Chou, Y.-H.; Chou, C.-H.; Chen, F.-C.; Lu, T.-C., Lasing behaviors upon phase transition in solution-processed perovskite thin films. *Appl. Phys. Lett.* **2014,** *105*, 231108.
25. Dhanker, R.; Brigeman, A. N.; Larsen, A. V.; Stewart, R. J.; Asbury, J. B.; Giebink, N. C., Random lasing in organo-lead halide perovskite microcrystal networks. *Appl. Phys. Lett.* **2014,** *105*, 151112.
26. Wu, K.; Bera, A.; Ma, C.; Du, Y.; Yang, Y.; Li, L.; Wu, T., Temperature-dependent excitonic photoluminescence of hybrid organometal halide perovskite films. *Phys. Chem. Chem. Phys.* **2014,** *16*, 22476-22481.
27. Even, J.; Pedesseau, L.; Katan, C., Analysis of multivalley and multibandgap absorption and enhancement of free carriers related to exciton screening in hybrid perovskites. *J. Phys. Chem. C* **2014,** *118*, 11566–11572.
28. Hirasawa, M.; Ishihara, T.; Goto, T.; Uchida, K.; Miura, N., Magnetoabsorption of the lowest exciton in perovskite-type compound (CH_3NH_3)PbI_3. *Phys. Rev. B* **1994,** *201*, 427–430.
29. Hsiao, Y.-C.; Wu, T.; Li, M.; Liu, Q.; Qin, W.; Hu, B., Fundamental physics behind high-efficiency organo-metal halide perovskite solar cells. *J. Mater. Chem. A* **2015,** *3*, 15372-15385.
30. von der Osten, W.; Stolz, H., Localized exciton states in silver halides. *J. Phys. Chem. Solids* **1990,** *51*, 765–791.
31. Williams, R.; Song, K., The self-trapped exciton. *J. Phys. Chem. Solids* **1990,** *51*, 679–716.
32. Yamada, Y.; Nakamura, T.; Endo, M.; Wakamiya, A.; Kanemitsu, Y., Near-band-edge optical responses of solution-processed organic-inorganic hybrid perovskite $CH_3NH_3PbI_3$ on mesoporous TiO2 electrodes. *Appl-Phys. Express* **2014,** *7*, 032302.
33. Arora, N.; Dar, M. I.; Hezam, M.; Tress, W.; Jacopin, G.; Moehl, T.; Gao, P.; Aldwayyan, A. S.; Deveaud, B.; Grätzel, M.; Nazeeruddin, M. K., Photovoltaic and amplified spontaneous emission studies of high-quality formamidinium lead bromide perovskite films. *Adv. Funct. Mater.* **2016,** *26*, 2846–2854
34. Oku, T., Crystal structures of $CH_3NH_3PbI_3$ and related perovskite compounds used for solar cells. **2015**; p 77-101.
35. Santamaria-Perez, D.; Chulia-Jordan, R., Compression of mineral barite, BaSO4: a structural study. *High Pressure Research* **2011,** *32*, 81-88.
36. Santamaria-Perez, D.; Kumar, R. S.; Dos Santos Garcia, A. J.; Errandonea, D.; Chulia-Jordan, R.; Saez-Puche, R.; Rodriguez-Hernandez, P.; Muñoz, A., High-pressure transition to the post-barite phase in BaCrO4 hashemite. *Physical Review B* **2012,** *86*, 94 - 116.
37. Santamaria-Perez, D.; Gracia, L.; Garbarino, G.; Beltran, A.; Chulia-Jordan, R.; Gomis, O.; Errandonea, D.; Ferrer-Roca, C.; Martinez-Garcia, D.; Segura, A., High-pressure study of the behavior of mineral barite by X-ray diffraction. *Phys. Rev. B* **2011,** *84*, 054102.
38. Saito, K.; Kurosawa, T.; Akai, T.; Yokoyama, S.; Morioka, H.; Oikawa, T.; Funakubo, H., Characterization of epitaxial Pb(Zrx,Ti1-x)O3 thin films with composition near the morphotropic phase boundary. *MRS Proc.* **2002,** *748*, U13.4.
39. Yokoyama, S.; Honda, Y.; Morioka, H.; Oikawa, T.; Funakubo, H.; Iijima, T.; Matsuda, H.; Saito, K., Large piezoelectric response in (111)-oriented epitaxial Pb(Zr,Ti)O3 films consisting of mixed phases with rhombohedral and tetragonal symmetry. *Appl. Phys. Lett.* **2003,** *83*, 2408–2410.
40. Kelman, M. B.; McIntyre, P. C.; Hendrix, B. C.; Bilodeau, S. M.; Roeder, J. F.; Brennan, S., Structural analysis of coexisting tetragonal and rhombohedral phases in polycrystalline Pb(Zr0.35Ti0.65)O3 thin films. *J. Mater. Res.* **2003,** *18*, 173-179.
41. Zeches, R. J.; Rossell, M. D.; Zhang, J. X.; Hatt, A. J.; He, Q.; Yang, C.-H.; Kumar, A.; Wang, C. H.; Melville, A.; Adamo, C.; Sheng, G.; Chu, Y.-H.; Ihlefeld, J. F.; Erni, R.; Ederer, C.; Gopalan, V.; Chen, L. Q.; Schlom, D. G.; Spaldin, N. A.; Martin, L. W.; Ramesh, R., A strain-driven morphotropic phase boundary in BiFeO3. *Science* **2009,** *326*, 977-980.
42. Chen, Z.; You, L.; Huang, C.; Qi, Y.; Wang, J.; Sritharan, T.; Chen, L., Nanoscale domains in strained epitaxial BiFeO3 thin Films on LaSrAlO4 substrate. *Appl. Phys. Lett.* **2010,** *96*, 252903.
43. Ehm, L.; Borkowski, L. A.; Parise, J. B.; Ghose, S.; Chen, Z., Evidence of tetragonal nanodomains in the high-pressure polymorph of BaTiO3. *Appl. Phys. Lett.* **2011,** *98* (2).
44. Wehrenfennig, C.; Liu, M.; Snaith, H. J.; Johnston, M. B.; Herz, L. M., Homogeneous emission line broadening in the organo lead halide perovskite $CH_3NH_3PbI_{3-x}Cl_x$. *J. Phys.Chem.Lett.* **2014,** *5* 1421-1426.
45. Zhang, H.; Banfield, J. F., Thermodynamic analysis of phase stability of nanocrystalline titania. *J. Mater. Chem.* **1998,** *8*, 2073–2076.
46. Chirvony, V. S.; González-Carrero, S.; Suárez, I.; Galian, R. E.; Sessolo, M.; Bolink, H. J.; Martínez-Pastor, J. P.; Pérez-Prieto, J., Delayed Luminescence in Lead Halide Perovskite Nanocrystals. *J. Phys. Chem. C* **2017,** *121*, 13381-13390.
47. Zhang, Y.; Yin, J.; Parida, M. R.; Ahmed, G. H.; Pan, J.; Bakr, O. M.; Brédas, J.-L.; Mohammed, O. F., Direct-indirect nature of the bandgap in lead-free perovskite nanocrystals. *J. Phys. Chem. Lett.* **2017,** *8*, 3173–3177.
48. Kiba, T.; Mizushima, Y.; Igarashi, M.; Huang, C.-H.; Samukawa, S.; Murayama, A., Temperature dependence of time-resolved photoluminescence in closely packed alignment of Si

nanodisks with SiC barriers. *Nanoscale Research Letters* **2013,** *8*, 223.
49. Weller, M. T.; Weber, O. J.; Henry, P. F.; Di Pumpo, A. M.; Hansen, T. C., Complete structure and cation orientation in the perovskite photovoltaic methylammonium lead iodide between 100 and 352 K. *Chem. Commun.* **2015,** *51*, 4180.
50. Wasylishen, R. E.; Knop, O.; Macdonald, J. B., Cation rotation in methylammonium lead halides. *Solid State Commun.* **1985,** *56*, 581–582.
51. Quarti, C.; Mosconi, F.; De Angelis, F., Interplay of orientational order and electronic structure in methylammonium lead iodide: Implications for solar cell operation. *Chem. Mater.* **2014,** *26*, 6557–6569.
52. Rudin, S.; Reinecke, T. L.; Segall, B., Temperature-dependent exciton linewidths in semiconductors. *Phys. Rev. B: Condens. Matter Mater. Phys.* **1990,** *42*, 11218–11231.
53. Pedrueza, E.; Segura, A.; Abargues, R.; Bosch, J.; Martínez-Pastor, J. P., The effect of quantum size confinement on the optical properties of PbSe nanocrystals as a function of temperature and hydrostatic pressure. *Nanotechnology* **2013,** *24*, 205701.
54. Varshni, Y. P., Temperature dependence of the energy gap in semiconductors. *Physica* **1967,** *34*, 149-154.
55. Pässler, R., Basic model relations for temperature dependencies of fundamental energy gap in semiconductors. *Phys. Status Solidi B* **2001,** *200*, 155–172.
56. Lautenschlager, P.; Garriga, M.; Logothetidis, S.; Cardona, M., Interband critical points of GaAs and their temperature dependence. *Phys. Rev. B* **1987,** *35*, 9174–9189.
57. Dey, P.; Paul, J.; Bylsma, J.; Karaiskaj, D.; Luther, J. M.; Beard, M. C.; Romero, A. H., Origin of the temperature dependence of the band gap of PbS and PbSe quantum dots. *Solid State Commun.* **2013,** *165*, 49–54.
58. Chen, Z.; Yu, C.; Shum, K.; Wang, J. J.; Pfenninger, W.; Vockic, N.; Midgley, J.; Kenney, J. T., Photoluminescence study of polycrystalline CsSnI3 thin films: Determination of exciton binding energy. *J. Lumin.* **2012,** *132*, 345–349.
59. Savenije, T. J.; Ponseca, C. S.; Kunneman, L.; Abdellah, M.; Zheng, K.; Tian, Y.; Zhu, Q.; Canton, S. E.; Scheblykin, I. G.; Pullerits, T.; Yartsev, A.; Sundström, V., Thermally activated exciton dissociation and recombination control the carrier dynamics in organometal halide perovskite. *J. Phys. Chem. Lett.* **2014,** *5*, 2189–2194.
60. Tanaka, K.; Takahashi, T.; Ban, T.; Kondo, T.; Uchida, K.; Miura, N., Comparative study on the excitons in lead-halide-based perovskite-type crystals $CH_3NH_3PbBr_3$ $CH_3NH_3PbI_3$. *Solid State Commun.* **2003,** *127*, 619–623.
61. Manser, J. S.; Kamat, P. V., Band filling with free charge carriers in organometal halide perovskites. *Nat. Photonics* **2014,** *8*, 737–743.
62. Yamada, K.; Mikawa, K.; Okuda, T.; Knight, K. S., Static and dynamic structures of $CD_3ND_3GeCl_3$ studied by TOF high resolution neutron powder diffraction and solid state NMR. *J. Chem. Soc., Dalton Trans.* **2002**, 2112–2118.

TABLES.

Table 1. Temperature coefficient of $CH_3NH_3PbI_3$ obtained for different fluences-excitations

Power (nJ/cm^2)	$\alpha = \partial E/\partial T$ $(\mu eV/K)$		
	Sub-Low	High = Orthorhombic	Low = Tetragonal
370	-38(7)	370(50)	-38(5)
23.8	-86(12)	24(4)	-86(9)
1.43	-388(70)	1.4(0.2)	-388(60)

Table 2. Bandgap Energy of $CH_3NH_3PbI_3$

Crystal Structure	Calculated Eg_o (eV) [34]	Measured Eg_o (eV)			
		370 nJ/cm^2	23.8 nJ/cm^2	1.43 nJ/cm^2	Deconvolution
Monoclinic		1.564(7)	1.524(3)	1.505(5)	1.491(13)
Orthorhombic	1.61	1.634(7)	1.628(4)	1.633(3)	1.613(4)
Tetragonal	1.43	1.5274(12)	1.529(2)	1.5286(14)	1.535(3)
Cubic	1.3				1.415(8)

Table 3. Temperature coefficient of $CH_3NH_3PbI_3$ obtained for the different temperature regions

T (K)	$\alpha = \partial E/\partial T$ (μeV/K)			
	Orthorhombic	Tetragonal	Monoclinic	Cubic
45.5 K	396(30)	455(14)	291(30)	147(20)
165 K	-164(50)	-168(30)	13(60)	
300 K	535(50)	235(13)	147(17)	236(19)

Table 4. Binding energy

Power (nJ/cm^2)	E_B (meV)					
	Sub-Low		Orthorhombic		Tetragonal	
	T < 165 K	T > 165 K	T < 165 K	T > 165 K	T < 115 K	T > 115 K
370	39(12)	5(6)	24(16)	3(4)	7(5)	11(7)
23.8	147(30)	9(5)	57(14)	3(2)	13(7)	9(4)
1.43	482(80)	12(5)	70(20)	2(2)	30(11)	6(4)

Insert Table of Contents artwork here

TOC GRAPHIC

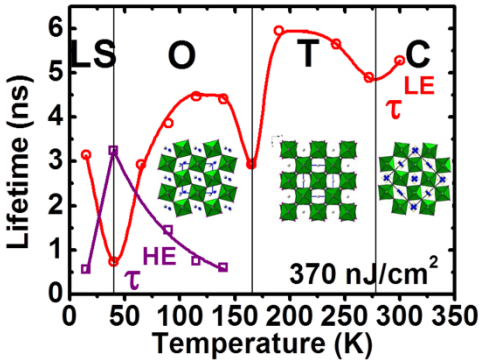
LS
O
T
C
LE
τ
HE
τ
370 nJ/cm2
Lifetime (ns)
Temperature (K)
0
1
2
3
4
5
6
0
50
100
150
200
250
300
350